Ca^{2+} imaging of neurons in freely moving rats with automatic post hoc histological identification

Philip Anner[a,b,*], Johannes Passecker[b], Thomas Klausberger[b], Georg Dorffner[a]

[a] Section for Artificial Intelligence and Decision Support, Center for Medical Statistics, Informatics and Intelligent Systems, Medical University of Vienna, 1090 Vienna, Austria
[b] Department of Cognitive Neurobiology, Center for Brain Research, Medical University of Vienna, 1090 Vienna, Austria

GRAPHICAL ABSTRACT
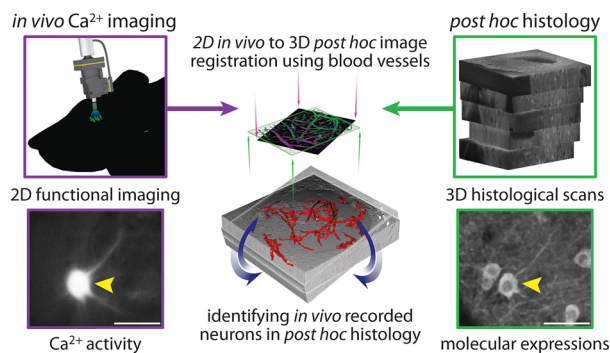
ARTICLE INFO

ABSTRACT

Background: Cognitive neuroscientists aim to understand behavior often based on the underlying activity of individual neurons. Recently developed miniaturized epifluorescence microscopes allow recording of cellular calcium transients, resembling neuronal activity, of individual neurons even in deep brain areas in freely behaving animals. At the same time, molecular markers allow the characterization of diverse neuronal subtypes by *post hoc* immunohistochemical labeling. Combining both methods would allow researchers to increase insights into how individual neuronal activity and entities contribute to behavior.

New method: Here, we present a novel method for identifying the same neurons, recorded with calcium imaging using a miniaturized epifluorescence microscope, *post hoc* in fixed histological sections. This allows immunohistochemical investigations to detect the molecular signature of *in vivo* recorded neurons. Our method utilizes the structure of blood vessels for aligning *in vivo* acquired 2D images with a reconstructed 3D histological model.

Results: We automatically matched, 60 % of all *in vivo* recorded cells *post hoc* in histology. Across all animals, we successfully matched 43 % to 89 % of the recorded neurons. We provide a measure for the confidence of matched cells and validated our method by multiple simulation studies.

Comparison with existing methods: To our knowledge, we present the first method for matching cells, recorded

* Corresponding author at: Section for Artificial Intelligence and Decision Support, Center for Medical Statistics, Informatics and Intelligent Systems, Medical University of Vienna, 1090 Vienna, Austria.
 E-mail address: philip.anner@meduniwien.ac.at (P. Anner).

with a miniaturized epifluorescence microscope in freely moving animals, *post hoc* in histological sections.
Conclusions: Our method allows a comprehensive analysis of how cortical circuits relate to freely moving animal behavior by combining functional activity of individual neurons with their underlying histological profiles.

1. Introduction

Modern cognitive neuroscience aims to determine how neuronal circuits process information based on defined cell types and how these neural representations relate to behavior. Anatomical attributes, such as neuronal cell types, connectivity, axonal and dendritic distribution are inherently linked to neuronal activity (Kepecs and Fishell, 2014; Markram et al., 2004) and are usually assessed by *post hoc* immunohistochemical labeling of fixed tissue (DeFelipe et al., 2013; DeFelipe and Fariñas, 1992; Kepecs and Fishell, 2014; Zeng and Sanes, 2017). In contrast, functional organizations of cortical circuits, at single-cell resolution, are typically assessed during behavioral experiments in rodents.

Although extracellular electrophysiological recordings in freely moving animals have been conducted for years (O'Keefe and Dostrovsky, 1971), the potential for differentiating neuronal cell types based on their electrophysiological profiles is limited. Single-cell electrophysiological recordings with subsequent dye filling (juxtacellular recording) have been conducted to identify the *in vivo* recorded cell in *post hoc* histology (Lapray et al., 2012; Pinault, 1996; Tang et al., 2014). However, being able to label only a single cell limits its scalability and does not allow the study of neuronal assembly activity.

In recent years, additional methods to monitor neuronal cell activity have been pioneered, including *in vivo* measurement of intracellular somatic calcium concentration in neurons (*in vivo* calcium imaging) (Chen et al., 2013; Grienberger and Konnerth, 2012). In contrast to electrophysiological recordings, *in vivo* calcium imaging allows the indirect monitoring of neuronal activity at a large scale with single-cell resolution and provides precise spatial locations and specific footprints of recorded neurons. Genetically encoded calcium indicators (GECIs) have become widely used calcium reporters that can be expressed by viral transduction using stereotaxic injection in specific brain areas, or by expression in genetically modified animal lines. To study the activity of neuronal subtypes, GECIs can be expressed in specific cell types. In mice, a variety of transgenic animal lines with neuronal subtype-specific expression of calcium reporters are available (Daigle et al., 2018). However, for some behavioral paradigms, rats are preferred because of their endurance and different behavior (Iannaccone and Jacob, 2009). The number of transgenic rat lines with neuronal subtype-specific expression of calcium reporters is limited compared to transgenic mouse lines.

To ultimately relate cell-type-specific neuronal activity with behavior and map connections between neurons, *in vivo* measured neuronal activity and *post hoc* histology need to be combined. This has been achieved for two-photon laser scanning microscopy (2 P M) (Keller and Martin, 2015; Kerlin et al., 2010; Khan et al., 2018; Langer and Helmchen, 2012; Wilson et al., 2017). 2 P M has a high lateral and axial resolution, and due to optical sectioning, volumetric scans can be acquired, facilitating cell matching *post hoc* in histology. All authors report that they identified neurons *post hoc* in histology in a manual and time-consuming procedure. The major limitation with the use of 2 P M is that it requires animals to be head-fixed, limiting the number of behavioral tasks possible. In most cases, 2 P M only allows limited depth penetration into the brain.

To overcome these limitations, miniaturized versions of *in vivo* calcium imaging microscopes have been developed in recent years (Ziv and Ghosh, 2015). These lightweight one-photon calcium imaging microscopes (miniscopes) have lower resolution and lack optical sectioning compared to 2 P M. In contrast, they can be mounted on the head of freely moving animals and thus allow the study of neuronal

activity in behavioral paradigms that require freely-behaving rodents. Partly, due to the decreased image quality of miniscopes, *post hoc* identification of recorded cells has not yet emerged. Being able to identify and immunohistochemically analyze cellular identities following one-photon calcium imaging provides an additional layer of information to understand cortical circuits. In this study, we developed a novel method to automatically identify neurons, recorded with a one-photon miniscope in freely moving rats, in *post hoc* histology. In contrast to manual identification approaches, our automatic cell matching algorithm is feasible to be used for large scale calcium imaging data that would be time-consuming, impractical, and difficult for manual cell matching. We focus on rats as here a cell-specific expression of genetically encoded calcium indicators is currently more limited and thus provides a potentially more significant benefit to the scientific community. We combine cell activity recordings by *in vivo* calcium imaging with a 3D-histological model developed from *post hoc* sections of the brain at the recording site. This facilitates the immunohistochemical characterization of *in vivo* recorded neurons and connectivity pattern analysis by using anterograde and retrograde neuroanatomical tracers. Our method allows a comprehensive analysis of neuronal circuits during flexible freely moving behavior by combining information about topographic specificity (localizing recorded cells), with cell-type specificity (neuronal identity using immunohistochemistry), and functional specificity (recorded calcium transients).

2. Materials and methods

All animal procedures were performed under an approved license by the Austrian Ministry of Education, Science and Research, and the Ethical Committee of the Medical University of Vienna. All data reported were obtained from five male Long Evans rats (320–400 g, three to four months at the time of surgery, acquired from Janvier Laboratories.

2.1. Virus injection and lens implantation

For all surgical procedures, rats were anesthetized with a mix of oxygen and isoflurane (Forane®, AbbVie, induction: 5 %, maintenance 2 %, oxygen flow: 2 L/min). The heads were shaved, and animals were fixated in a stereotaxic frame (Narishige). An iodine solution was used to disinfect the surgery site, and Vita-Pos® (Ursapharm) was applied to the eyes. Local anesthetics (Xylocaine® 2 %, Aspen) and systemic analgesics (Metacam® 2 mg/mL, 0.5 mL/kg, Boehringer Ingelheim) were applied. Body temperature was monitored, and a heating pad was used to maintain core body temperature at 37 °C during the procedure. Every 2 h, 2 mL Ringer solution (B. Braun) was injected subcutaneously to prevent dehydration. The surface of the cranium was exposed, and the periosteum and nearby muscle tissue were removed. The area was washed with a sterile Ringer solution, and six stainless steel screws were anchored into the cranium to provide stability for a head-mounted construct, fixing the endoscopic relay gradient-index (GRIN) lens and the miniscope holder. A craniotomy was performed (anterior-posterior (AP): +2.5 mm to 4 mm, medio-lateral (ML): 0.2 mm–1.5 mm) to provide access for virus injections and lens implantation, followed by carefully removing the dura. A saline solution was applied to avoid surface edemas. Calcium indicators (rAAV2/1-SynI-GCaMP6f, rAAV9/1-SynI-GCaMP6f, Univ. Pennsylvania Vector core) were injected at 12 sites into the prelimbic cortex (coordinates: ML: +2.9 mm, +3.5 mm, AP: +2.9 mm, +3.5 mm, dorso-ventral (DV): 2.4 mm, 2.7 mm,

3.0 mm). GRIN lenses (0.6 mm diameter, 6.1 mm length, ProView™ lens, Inscopix) were implanted with a stepper motor (Inchworm® 8200, EXFO, speed: 1 μm/second, coordinates: AP: +2 mm, ML: +0.7 mm, DV: 2.5 mm) using a ProView™ lens holder Kit (Inscopix). The craniotomy site was sealed with a silicone elastomer (Kwik-Sil™, World Precision Instruments). Head caps were built out of bone cement (Refobacin®, Biomet) and blue light–sensitive cement (Tetric EvoFlow®, ivoclar vivadent). A custom made camera holder was mounted with cement on top of the head cap. If necessary, sutures were applied, and the area was disinfected with iodine solution. Animals were given at least 14 days of recovery time.

2.2. Freely-moving calcium imaging

Once animals fully recovered, they were habituated for three days to the experimenter and the behavioral recording room. Two animals were recorded on an elevated wooden Y-maze. The maze was 55 cm in height, and the size of each arm was 80 × 11 cm. Three rats were recorded in a square open-field arena (90 × 90 × 30 cm) made of black painted wood. All animals were given sugar pellets (TestDiet®) as random rewards. Animals were recorded for ∼ 20 min, 5–15 times. We used a commercially available miniaturized epifluorescence microscope (Inscopix) to record neuronal activity at a rate of 20 Hz. Digital gain (∼ 1.5) and LED intensity (∼ 0.8 mW) were adjusted to maximize the dynamic range for each animal. The optical focus was kept the same among the recordings. We used nVista (Inscopix) to record calcium imaging experiments.

2.3. Histology

Following freely-moving experiments, rats were deeply anesthetized with urethane and transcardially perfused with saline followed by 20 min of fixation (4 % paraformaldehyde v/v, 15 % saturated picric acid v/v and 0.05 % glutaraldehyde w/v in 0.1 M phosphate buffer at pH 7.2). Camera holders were removed, and craniums were fixated in a stereotaxic apparatus. Endoscopic lenses were fixed to a stereotaxic arm with super glue and detached from the cement construct using a mini drill (Microtorque). We extracted the lenses using the stereotaxic arm. After brain extraction, axial sections were cut at 70 μm with a vibratome (Leica). Sections were washed in phosphate buffer and incubated in rabbit anti-GFP monoclonal antibody (Invitrogen, 1:20000, incubated for 5 days at 4 °C) and anti-rabbit conjugated to Alexa Fluor® 488 (Jackson ImmunoResearch Laboratories, 1:1000, incubated 4 h at room temperature). Images were acquired with an inverted laser confocal microscope (Leica TCS SP5).

2.4. Analysis and statistics

In all analyses, alpha is 0.05, and statistical testing was two-tailed, unless stated otherwise. Descriptive statistics were used to check for approximate normal distributions. T-tests were used to compare normally distributed data. Otherwise, Mann–Whitney U tests were used. For comparisons between more than two groups, the one-way ANOVA with Tukey Kramer *post hoc* test was used. For correlations, the Pearson correlation coefficient was used. Bonferroni correction was used to account for alpha error accumulation in multiple testing. All statistical analyses and image processing procedures were done using Matlab (MathWorks®) R2018a.

2.5. Image processing

2.5.1. In vivo calcium imaging movies

We used Mosaic (Inscopix) software to process calcium imaging recordings. First, we down-sampled calcium imaging movies (to 721 × 521 pixels), applied a Gaussian filter (σ = 0.5), and performed image registration (minimizing translations) to compensate for

movements. Neurons were identified using PCA/ICA analysis (Mukamel et al., 2009).

2.5.2. Temporal tracking of the same cells and shape segmentation

To align individual calcium imaging recordings, we calculated minimum intensity projection images (minIP) of the movies. minIPs depict the structure of blood vessels and we co-registered the minIP images of all recordings. We used the transformation parameters, obtained for each recording by minIP alignment, and applied them to the spatial cellular footprints recorded in each calcium imaging session. We applied an image registration method consisting of a local motion model, correcting for affine transformation, followed by a local motion model described by a free-form deformation (FFD) image registration based on B-splines (Rueckert et al., 1999). As a similarity measure, we used the normalized sum of squared differences (SSD) and provided manually defined control points. We registered all images of the recordings (minIP and neuronal footprints) to the same coordinate system.

We automatically segmented the shape of all recorded cells using the individual independent component images derived from the Mosaic software. Cell somata were identified by adaptive global image thresholding using Otsu's method, followed by morphological opening. Dendritic structures were detected by a morphological top-hat transform, multiple image convolution procedures, and region growing (Kellner, 2011). Total cell areas thus combined segmented somatic and dendritic structures.

Following alignment of the calcium imaging recordings, small shifts across the aligned images were still present. These small shifts between images impeded tracking of the same cells across days. To account for these inaccuracies in the process of identifying the same cells across recordings, we convolved the centroid of all segmented somatic areas by a Gaussian kernel and calculated joint probability density functions (PDFs) of all possible cell pairs across calcium imaging recordings. The same cells were matched according to the highest joint PDF value, and a minimum joint PDF based threshold for accepting cell matches was determined empirically. The threshold affected the distance of cell pairs being considered for matching and therefore depended on the precision of the image registration between the individual *in vivo* Ca2+ imaging recordings. As displacements between *in vivo* Ca2+ imaging recordings differed, a cell from recording 1 may be identified in recording 2, and the cell from recording 2 may be identified in recording 3. Due to displacements, the cell from recording 1 may not be identified in recording 3. To compensate for these displacement-induced errors, we calculated the transitivity of all matched cells between the *in vivo* Ca2+ imaging recordings.

2.5.3. Blood vessel detection in vivo

Following freely moving calcium imaging experiments, we visualized blood vessels in anesthetized rats by injecting a fluorescent dye *via* tail vein injection. Pre-processing of the movies was performed the same way as for the freely moving calcium imaging experiments. We recorded three minute long movies before and following fluorescent dye injection (Uranine AP, 0.8 mg/mL, 10 mL/kg, Merck) and calculated standard deviation projection images. To detect blood vessels, we calculated a digitally subtracted angiogram (DSA), a well-established method in interventional radiology. We subtracted the pre-contrast image (before dye injection) from the image acquired with the dye injected, followed by morphological bottom-hat filtering and segmentation based on the second local order structure of the image (Frangi et al., 1998). We refer to this image as DSA_{seg}.

2.5.4. 3D histology reconstruction and segmentation

Images of individual stacks were pre-processed (intensity scaling, noise reduction by Wiener filtering, and 2D median filtering (4 × 4 neighborhood)) and we calculated maximum intensity projections (maxIP) of images close to the dorsal and ventral borders of the image

stacks to compensate for a localized loss of information. The imaging site was estimated based on the GRIN lens-induced lesion and the co-ordinates along the medio-lateral and anterior-posterior axes. We derived image registration parameters for neighboring sections by co-registering the last (ventral) maxIP image of the first stack and the first (dorsal) maxIP image of the second stack. The images were co-registered using free-form deformation alignment (Rueckert et al., 1999), and resulting transformation parameters were applied to all images of the second image stack.

Due to the low signal-to-noise ratio for the detection of GCaMP6f expression, we manually segmented cell somata of GCaMP6f positive cells. Based on manually segmented somata, we automatically segmented dendritic structures by 3D morphological operations (top-hat filter, 3D convolution, and adaptive thresholding). For multimodal 2D to 3D alignment, we calculated maxIP images of individual 3D segmented cell structures.

To segment blood vessels in histology we adjusted the contrast of the image stack with contrast-limited adaptive histogram equalization (CLAHE), followed by Gaussian filtering ($\sigma = 2$), morphological bottom-hat transform, and volumetric image segmentation based on the second local order structure of the image stack (Frangi et al., 1998). We refer to volumetric segmented blood vessels in *post hoc* histology as V_{seg}.

2.5.5. Multimodal image alignment based on blood vessels

We co-registered *in vivo* and *post hoc* imaging modalities based on the structure of blood vessels captured *in vivo* (DSA_{seg}) and in *post hoc* histology (V_{seg}).

For V_{seg}, we calculated a maxIP image and performed basic alignment. Basic alignment was achieved by providing at least two manually defined non-collinear control points to solve a linear equation system for translating, rotating, and scaling DSA_{seg} to fit the vascular structure of maxIP of V_{seg}. Following basic alignment, we refined the axial projection distance for maxIP of V_{seg} by carefully comparing the blood vessel patterns to the aligned DSA_{seg} image.

To account for a potential misalignment of the imaging plane acquired *in vivo* and the angle of *post hoc* cut sections, we estimated rotation parameters between the images to maximize the overlap of segmented blood vessels detected in DSA_{seg} and maxIP of V_{seg} quantified by the Jaccard index. When cutting the fixed brains, we aimed to cut them in parallel to the imaging plane of the implanted endoscopic lens. Therefore, we assumed that the misalignment was limited to a small range ($\pm 10°$). As blood vessels detected *in vivo* and *post hoc* do not represent a bijective relation, we assume that maximal Jaccard values with rotations outside $\pm$ 10° result due to the ambiguous alignment of blood vessels. We calculated the rotations of the 3D histology model at 0.5° steps from -25° to +25° and obtained maximal Jaccard values with rotation parameters α (rotation along the x-axis) and β (rotation along the y-axis) by

$$\widehat{J} = \underset{\alpha,\beta}{\operatorname{argmax}} \operatorname{Jac}(DSA_{seg}, maxIP(V_{seg} \times R_x(\alpha) \times R_y(\beta)))$$

where R_x and R_y are rotation matrices,

$$R_x(\alpha) = \begin{bmatrix} 1 & 0 & 0 \\ 0 & \cos \alpha & -\sin \alpha \\ 0 & \sin \alpha & \cos \alpha \end{bmatrix}$$

$$R_y(\beta) = \begin{bmatrix} \cos \beta & 0 & \sin \beta \\ 0 & 1 & 0 \\ -\sin \beta & 0 & \cos \beta \end{bmatrix}$$

and *Jac* refers to the Jaccard index of binarized segmented blood vessel structures. If maximal Jaccard values were found to be outside the assumed range of $\pm 10°$, we concluded that this resulted due to ambiguous alignment and used the non-rotated models for final alignment. Otherwise, we rotated histological image stacks by rotation matrices $R_x(\alpha)$ and $R_y(\beta)$ that maximized the Jaccard index and used Nearest-

neighbor interpolation to assign pixel values. For final alignment, we used maxIP of V_{seg} (either from rotated or non-rotated V_{seg}) and applied FFD transformations to align DSA_{seg}, by providing manually defined control points and maximizing normalized cross-correlation between the images.

To account for inaccuracies following image registration, we quantified potential offsets between aligned blood vessel structures in DSA_{seg} and maxIP of V_{seg} and incorporated them as prior knowledge in our cell matching algorithm. To detect even small offsets, we calculated morphological skeletons of blood vessels that resembled their central lines. We used Sobel operators for generating orientation-based skeleton blood vessel models (vertical and horizontal), and calculated inverse distance transforms of them. Using image gradients, we determined the closest point in DSA_{seg} skeleton blood vessel models for each recorded cell. For each *in vivo* recorded cell we used image gradients to determine the closest point of the central lines of blood vessels in DSA_{seg}. From that point, we determined the distance to the closest blood vessel in histology (skeleton maxIP of V_{seg}) using image gradients of the horizontal and vertical models. The model resulting in the closest distance was used, as it was more likely to represent the offset accurately. However, as blood vessels in DSA_{seg} and maxIP of V_{seg} do not form bijective relationships; ambiguous distances of blood vessels may arose. To account for potential misalignments, we restricted distances of skeleton vessels in DSA_{seg} and maxIP of V_{seg} to be lower than the distance of a neighboring vessel in calcium imaging (DSA_{seg}). From the position of each *in vivo* recorded cell, we derived localized offsets of blood vessels. Individual offset estimations may be biased due to a wrong pairing of blood vessels evoked by the non-bijective relationship of blood vessel structures. Recorded cells in a close spatial distance were likely to be related to similar offsets of blood vessels. To reduce the influence of individually biased offset estimations from single cells, we identified spatial clusters of cells and derived cluster-based (mean) estimates of blood vessel offsets. Cell clusters were identified using k-means clustering. We increased the number of clusters until the Euclidean distance between all cells belonging to a cluster, and the centroid of the cluster was lower than a threshold. For calculating the threshold, we quantified the spatial distances between all recorded cells in calcium imaging and detected the closest neighbor for each cell. The maximum distance from all closest neighboring cells defined the threshold. For each cell cluster, we calculated the mean norm of the offset vectors. In the cell matching algorithm, we included blood vessel offset vectors as a Euclidean constraint for allowing displaced pairs of cells being matched.

2.6. Automatic multimodal cell matching

To match cells, that were recorded in *in vivo* calcium imaging (C_n), and were detected in *post hoc* histology (H_i), we calculated normalized (min-max normalization) 2D Euclidean distances (EUC) (along the anterior-posterior and medio-lateral axis), joint PDF of the 2D centroid positions (PDF), Jaccard indices for shape similarities of cell somata (JS), and Jaccard indices for total cell area (including dendritic structures) (JT) of all possible cell pairs between *in vivo* calcium imaging and *post hoc* histology. We automatically determined matching cells using a linear program and found maximal similarity scores *Sim* for all combinations of cell pairs C_n and H_i.

For each cell C_n in *in vivo* calcium imaging $n = (1,2,...,N)$,
and each cell H_i in *post hoc* histology $i = (1,2,...,M)$,

$$\underset{H_i, C_n \in \mathbb{N}}{\operatorname{argmax}} Sim(C_n, H_i) = PDF(C_n, H_i) + JS(C_n, H_i) + JT(C_n, H_i) - EUC(C_n, H_i),$$

where N is the number of cells recorded *in vivo*, and M is the number of cells segmented in *post hoc* histology. Cell shape similarity was evaluated by aligning cells based on their centroids, followed by calculating Jaccard indices $JS(C_n, H_i)$ and $JT(C_n, H_i)$, and weighting them with $PDF(C_n, H_i)$. The similarity score (*Sim*) for matched cell pairs (C_n, H_i)

can be interpreted as a criterion for the confidence of a matched cell pair. Hypothetically, a perfectly matched cell would result in a similarity score of 3. To simplify the interpretation of the similarity scores, we normalized them to a maximum value of 1 by dividing them by 3. Cell matching of (C_n) and (H_i) is exclusive. Each cell recorded in *in vivo* calcium imaging can only be matched with one cell in histology and *vice versa*. To ensure uniqueness of cell matching, a hierarchy based on the ranking of similarity scores was introduced. Further, we defined local maximum 2D Euclidean distance thresholds for accepting cell pairs to be matched. The thresholds incorporate the average size of all in *vivo* recorded cells and localized offset vectors, quantifying local image registration offsets. For each cluster of *in vivo* recorded cells, we calculated the mean of the norm of the corresponding offset vectors. As distorted cells on the borders of the field of view can bias the estimations of cell radii, we calculated cell soma radii for somatic shapes with an eccentricity < 0.5 and minor axis length of fitted ellipsoids, otherwise.

For all matched cells in *post hoc* histology, we estimated the (dorsoventral) distance from the GRIN lens-induced lesion. To compare the distances of matched cells from the lesion across animals, we normalized the distances based on the estimated working distance, determined by the structure of blood vessels, captured with both imaging modalities.

Further, we aimed at investigating whether non-matched cells were rather located at the borders of the field of view. We assumed that the center of the field of view is represented by the spatial centroid of all *in vivo* recorded cells. To determine the spatial centroid of all *in vivo* recorded cells, we performed k-means clustering of all cell soma centroids. K-means clustering was performed with only one cluster. Subsequently, we determined the Euclidean distances between the centroid of all *in vivo* recorded cells and matched, as well as non-matched cells.

2.7. Validation of the cell matching method

Firstly, we performed a simulation study by artificially introducing an error for the *in vivo* acquired calcium imaging data by randomly rotating the images up to ± 45° in the x- and y-direction. With the error introduced, we performed image registration (basic alignment, rotation alignment, FFD alignment) and matched cells *post hoc*. We evaluated the number of matched cells and investigated whether we can match the same cell pairs as in the original error-free configuration. Secondly, we randomly rotated detected cells in a histology model along the x- and y-axis to introduce an error. With the error introduced, we matched cells between *in vivo* calcium imaging and the rotated histology without re-alignment and quantified the number of matched cells. Thirdly, we investigated the effect of missing blood vessels on the number of matched cells. We randomly removed connected blood vessels from *in vivo* calcium imaging until 10 %, 25 %, 50 %, and 75 % of the initially detected blood vessels were remaining. We asked three biologists to perform an alignment with the remaining blood vessel structures and evaluated the cell matching algorithm. Fourthly, we aimed to evaluate if the number of matched cells deviate from chance level. Therefore, we randomly displaced the positions of cells detected in histology and evaluated the numbers and similarity metrics of matched cells. We randomly translated all segmented cells along the anterior-posterior and medio-lateral axis 1000 times for each animal. The minimum translation distance was set to be larger than the maximum 2D Euclidean distance for accepting cell matches (mean cell diameter + the highest magnitude of the offset vectors from multimodal aligned blood vessels), assuring a reorganization of the original positions of the cells. Fifthly, due to the high density of neurons in histology, cells may be matched by chance. Therefore, we aimed at investigating the correlation between the numbers of cells detected in histology and the likelihood of matching cells by chance. To elucidate the effect of a high density cellular area in histology, we created a combined histology model by stacking histological 3D models of three
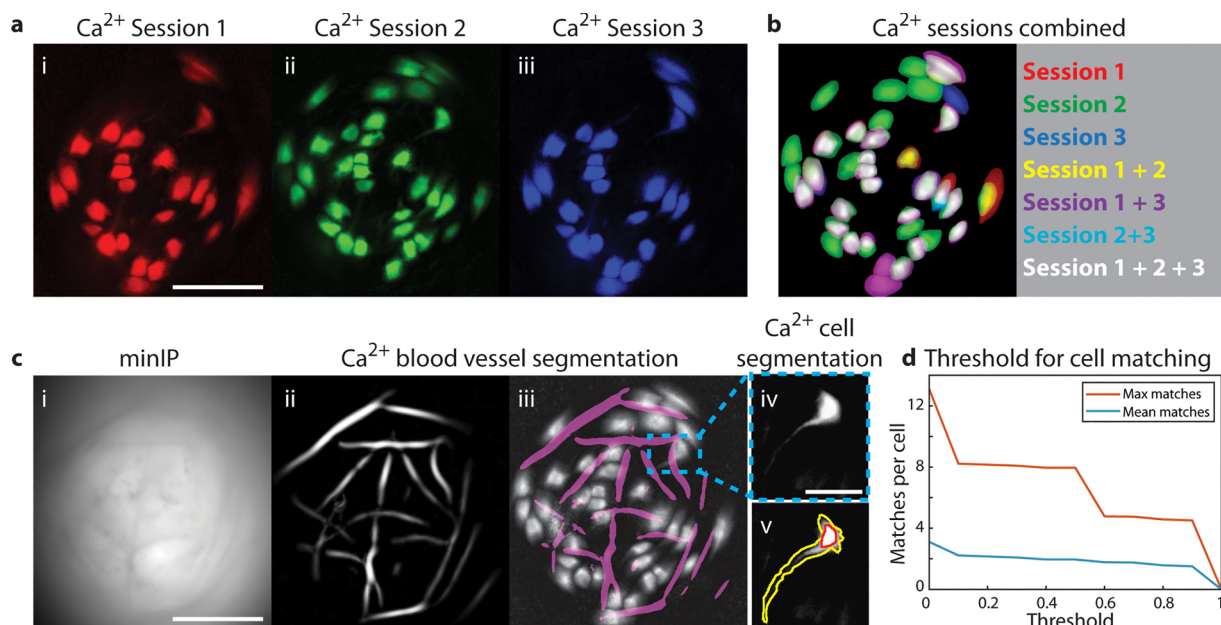

Fig. 1. Image processing of *in vivo* calcium imaging data. a) Spatial footprints of prefrontal neurons recorded in three individual Ca^{2+} imaging sessions indicated in red, green, and blue. Recordings were co-registered based on blood vessels found by temporal projections (minimum intensity projection) of the recordings (see Fig. 1c (i)). b) Red, green, and blue (RGB) overlay of combined cells of (a). c) (i) Minimum intensity projection (minIP) of a single Ca^{2+} recording. (ii) Automated segmentation of blood vessels following fluorescent dye injection *in vivo*. (iii) Co-registered and combined cells of three recording sessions overlaid with segmented blood vessels. Insert: (iv) Individual cell recorded *in vivo*. Scale bar is 50 μm. (v) Automatic segmentation results of total cell area (yellow) and cell soma (red). d) Various thresholds for minimum joint PDF values for accepting cells matched across 3 Ca2+ imaging sessions (from subfigure a). The blue curve depicts the mean of identified instances of all recorded cells across days. The red curve depicts the maximum number of instances identified across days for all cells. Gamma values have been adapted to enhance visualization of subfigures a, b, and c. All scale bars are 100 μm if not stated otherwise.

animals along the dorso-ventral axis. We selected histological models of animals with the highest number of cells located in *post hoc* histology. To compare the fraction, distance, and shape overlap of matched cells

at the chance level to the results we obtained within our experiments, we aligned calcium imaging data of two animals with the combined histology model. For evaluating the effect of the number of cells
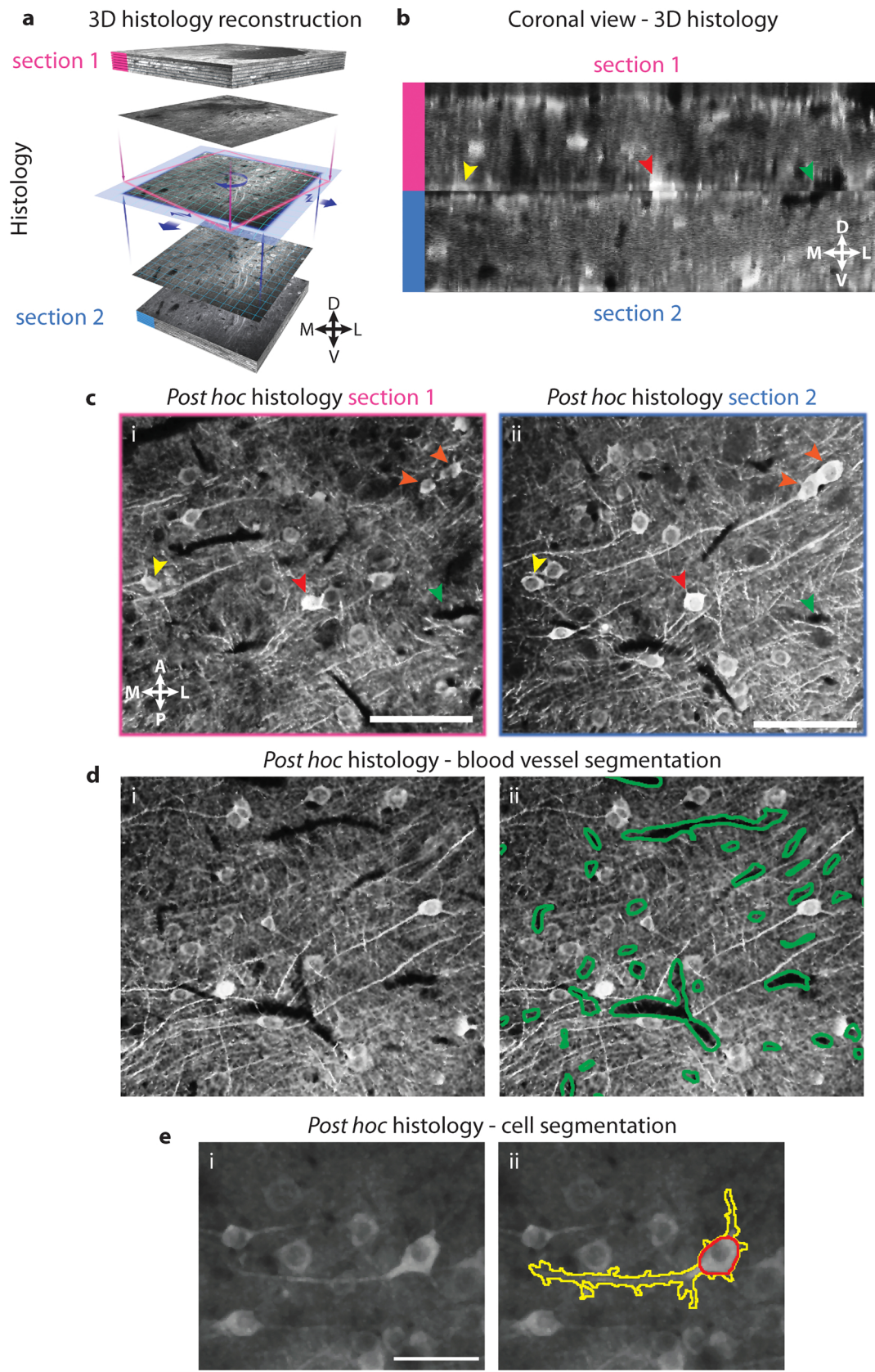
(caption on next page)

Fig. 2. Image processing of *post hoc* histology. a) Individual sections were 3D scanned with a laser confocal microscope. Alignment parameters of each neighboring image stack were achieved by 2D co-registration of the first and last image of each image sack. Acquired alignment parameters were used to transform all remaining images of the second image stack. b) Coronal view of some cells shown in c). Color-coded arrows highlight control points identified on both sections (first image stack – pink, second image stack - blue). c) Co-registration of the last image of the first image stack (pink) and the first image of the consecutive image stack (blue). Color-coded arrows indicate corresponding control points identified in both sections. d) Blood vessels were 3D segmented in the aligned model. An individual example image from the stack is visualized (left) and overlaid with segmented blood vessels in green (right). e) Cells were 3D segmented in the aligned histological model - automatic segmentation results of cell area (yellow) and cell soma (red). Scale bar is 50 μm. All scale bars are 100 μm if not stated otherwise. Anatomical orientations are defined along anterior (A)-posterior (P), medio (M)-lateral (L), and dorso (D)-ventral (V) axes.

included in histology on *post hoc* cell matching, we matched cells for the two animals *post hoc* in cumulatively increasing subsamples (10 μm steps along the dorso-ventral axis) of the combined histology model. The aligned calcium imaging data of animal 1 was derived from the same animal as the first segment of the combined histology model. Therefore, animal 1 represented a non-random alignment within stack 1 of the combined histology model. Calcium imaging data of animal 2 was derived from a different animal that was not included in the combined histology model. Hence, animal 2 represented a random alignment within all segments of the combined histology model. We compared the fractions, distances, and spatial overlaps of matched cells for each subsample of the combined histology model between animal 1 and 2.

3. Results

Here, we present a cell matching procedure for identifying neurons recorded during one-photon *in vivo* calcium imaging with *post hoc* immunohistochemistry. To maximize the number of *in vivo* recorded cells, we tracked and combined cells recorded in multiple *in vivo* calcium imaging experiments. Using a fluorescent dye *in vivo*, we detected blood vessels during calcium imaging for the alignment with *post hoc* histology. Once animals were perfused, two consecutive histological brain sections covering the optical distance of the miniscope plane were used for 3D reconstruction of the imaging plane. We then performed multimodal image alignment based on the structure of blood vessels, identified *in vivo* and from *post hoc* histology. Following alignment, we automatically identified *in vivo* recorded cells in *post hoc* histology, allowing the determination of the cell-type-specific activity of individual neurons by *post hoc* immunohistochemical labeling.

3.1. Cell tracking across multiple days

The number of cells recorded in calcium imaging sessions varied across days (Fig. 1a), and combining multiple recordings increased the total number of recorded cells. Combining multiple calcium imaging recordings necessitated the co-registration of the calcium imaging recordings. We used the structure of blood vessels and calculated minIP images (Fig. 1c (i)) to align the calcium imaging movies (figure S1). Despite the co-registration of calcium imaging movies, minor offsets between the aligned spatial footprints of cells across recordings were still present. Individual cells were tracked across days by calculating joint PDFs based on the spatial centroid of their cell soma. A minimum joint PDF of 0.6 was determined empirically to account for misalignments following image registration to match the same cell across experiments (Fig. 1d). For three animals, three individual calcium imaging recordings were combined (Fig. 1b). For one additional animal, two calcium imaging recordings were combined, and for another animal, cells were identified in a single calcium imaging recording. In total, 225 cells were recorded in five animals. In the animals where we combined cells from three recordings (136 cells), we detected 40 % (55 cells) in one recording, 38 % (51 cells) in two recordings, and 22 % (30 cells) across three recordings.

3.2. Blood vessel detection and cell segmentation in vivo

We observed that minIP images were restricted to superficial blood vessels and would not allow reliable matching with *post hoc* histology. Injection of a fluorescent dye *in vivo*, followed by a DSA calculation and automatic segmentation of blood vessels, allowed a precise detection of blood vessel structures *in vivo* (Fig. 1c (ii), (iii)). Automatic segmentation of somatic and total cell areas, including dendritic structures, allowed the detection of spatial footprints from all *in vivo* recorded cells for *post hoc* cell matching (Fig. 1c (iv), (v)).

3.3. 3D histology reconstruction

Identifying *in vivo* recorded cells *post hoc* required the reconstruction of a 3D histology model. The estimation of the miniscopes working distance, based on the structure of local blood vessels captured *in vivo* and *post hoc*, allowed the estimation of the number of histological sections required for the reconstruction of the histological 3D model. For three animals, we aligned two neighboring histological sections, and for two animals, the estimated working distance was covered within the first section. We compensated for observed non-linear deformations of neighboring histological sections by applying FFD image registration. Likely due to the cutting process, the borders of the sections were not coherently linear, resulting in localized loss of information in individual images close to the upper and lower borders of the acquired 3D scans. By applying maxIP of the corresponding images, we could correct for this loss of information. However, minor tissue was inherently lost during the brain cutting process, impeding the co-registration of adjacent sections. We achieved co-registration of consecutive histological sections (Fig. 2a) by using manually defined control points, indicating blood vessels, neurons, and cortical structures identified in both images (Fig. 2c) and applied the estimated 2D transformation parameters to all remaining images of section 2 (Fig. 2a). Alignment of the neighboring sections was visually assessed by elements identified across sections, such as blood vessels and cells, in the axial, coronal, and sagittal views (Fig. 2b,c). In the reconstructed 3D histology model we could automatically segment all blood vessels (Fig. 2d). Due to low contrasts and high signal-to-noise ratio, automatic segmentation failed. Therefore, we segmented cell somata in *post hoc* histology manually. Starting from somatic regions, using automatic segmentation we could capture fine dendritic structures and detected total cell areas (Fig. 2e). On average, we segmented 120.8 ± 58.7 cells in the volumes of interest per animal (mean $\pm$ Stdev).

3.4. Multimodal image alignment based on blood vessels

We achieved 2D to 3D alignment between *in vivo* calcium imaging (2D) and *post hoc* histology (3D), based on the structure of blood vessels (Fig. 3a). The basic alignment was achieved by providing at least two manually defined control points to solve the linear equation system for translating, rotating, and scaling DSA_{seg} to fit the vascular structure of maxIP of V_{seg}. In all animals, we obtained estimations of the miniscope's *in vivo* working distance by incrementally increasing the projection distance along the z-dimension of the 3D segmented histological blood vessels, until similar structures of blood vessels could be detected. We found that the blood vessels derived *in vivo* and post mortem did not
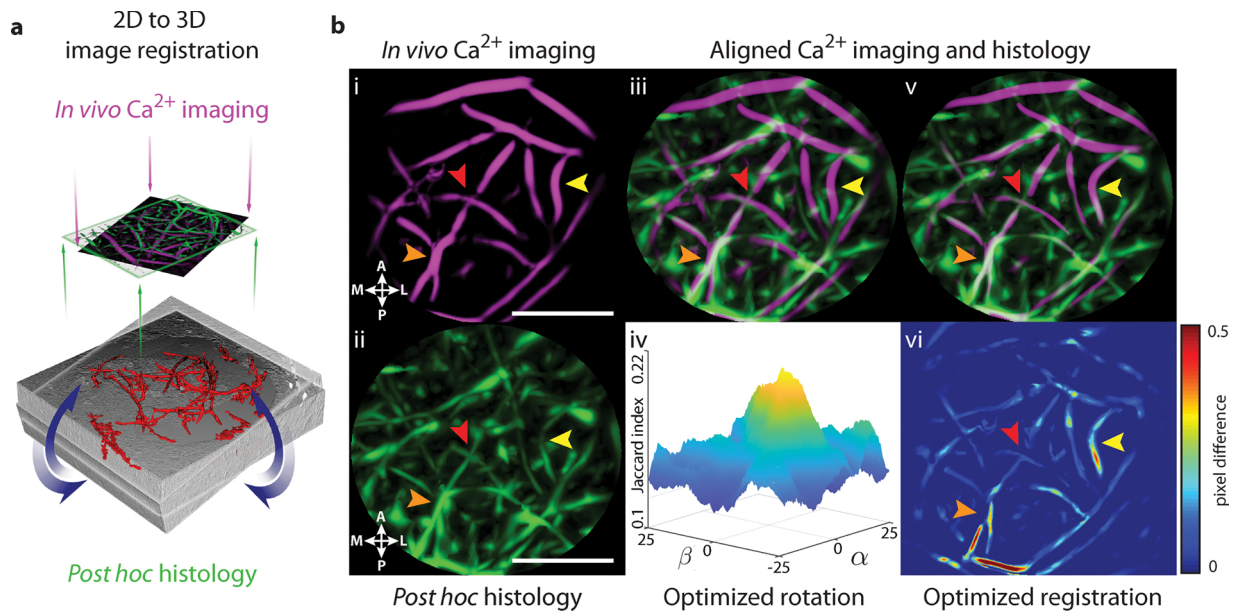
Fig. 3. Multimodal *in vivo* to *post hoc* image alignment based on blood vessels. a) Schematic drawing of the multimodal 2D-to-3D image registration. Registration is based on the local structure of blood vessels, captured with both imaging modalities (*in vivo* calcium imaging and *post hoc* histology). Blood vessels detected in the 3D histology model are projected onto a 2D image. Potential differences in projection angles of the blood vessels captured *in vivo* compared to histology were minimized by evaluating rotations of the 3D histology model. b) Alignment of *in vivo* acquired images of blood vessels (violet) and 2D projection of *post hoc* derived blood vessels (green). Colored arrows highlight control points identified across images. (i) Blood vessel detection following fluorescent dye injection during calcium imaging. (ii) 2D projection of *post hoc* derived blood vessels from 3D histology. (iii) Basic registration (translation, rotation, and scaling) of *in vivo* captured blood vessels (violet) and *post hoc* 2D projection of blood vessels identified in histology (green). (iv) Example depicting the optimization surface for rotations ranging from -25° to + 25° for α (rotation along the x-axis) and β (rotation along the y-axis) with a clearly defined peak at α = 1.5° and β = -4.5°. (v) Final alignment (2D–3D rotation alignment, followed by free-form deformation alignment) of *in vivo* and *post hoc* identified blood vessels. (vi) Pixel by pixel-wise multiplication of intensity values displays the difference in overlapping regions of basic *versus* final blood vessel alignment. Pixel intensity values were scaled from 0 to 1. All scale bars are 100 μm.

form a bijective relation. Some blood vessels captured *in vivo* could not be detected in *post hoc* histology and *vice versa*. Nevertheless, they allowed unambiguous co-registration of the imaging modalities (Fig. 3b (i), (ii), and (iii)). The mean estimated working distance based on *post hoc* detected blood vessels was 65.76 ± 31.59 μm (mean ± Stdev), notably lower than specified by construction (Jung and Schnitzer, 2003). The difference can be explained due to the shrinkage of brain tissue caused by fixation with formaldehyde (Kiessling and Pichler, 2011).

Following basic alignment (translation, rotation, and scaling; Fig. 3b (iii)), we maximized Jaccard indices by rotating *post hoc* histology for two out of five animals at (α = 1.5°; 9° and β = -4°; 3.5°, respectively) with a clearly defined peak at the optimum (example of one animal: Fig. 3b (iv)). For three animals, we did not find rotation parameters that maximized Jaccard indices within the assumed range of ± 10°. We concluded that maximal Jaccard indices did not necessitate rotations of the histology models. Subsequent FFD alignment allowed precise alignment of *in vivo* and *post hoc* acquired images (Fig. 3b (v)) and improved the basic alignment procedure (Fig. 3b (vi)). Matching of *in vivo* recorded cells in *post hoc* histology required *in vivo* calcium imaging data to be accurately aligned with *post hoc* histology. We found minor offsets in aligned blood vessels of the imaging modalities in five animals and quantified the offsets by measuring local distance offsets based on the structure of blood vessels, by 3.68 ± 4.07 μm (mean ± Stdev) and incorporated the offsets in our cell matching algorithm.

3.5. Multimodal cell matching

In five animals, out of 225 recorded neurons *in vivo*, we matched 140 cells (62.2 %) *post hoc* in histology. 85 cells (37.8 %) were not matched *post hoc* in histology. Cells were matched *post hoc* in all animals, and fractions of matched cells ranged from 43.3 % to 89.47 % (Fig. 4a). Similarity scores of matched cells were 0.47 ± 0.10 (Mean ± Stdev) and ranged from 0.23 to 0.70 (figure S2). We confirm

that individual cells show preserved shapes (somatic shapes and dendritic structures) between *in vivo* calcium imaging and *post hoc* histology (Fig. 4c–e).

The 2D–3D rotation optimization procedure, performed for two animals, affected a subset of *post hoc* matched cells by modifying the pairing of the cells. These cells were matched in non-rotated histology models to cells at a significantly higher dorso-ventral distance (corrected p = 0.006, Mann-Whitney U test) from the lesion compared to cells, whose pairing was not affected by rotation alignment. After rotation alignment, the cells affected by rotation alignment were matched to cells at a non-significantly different estimated dorso-ventral distance (corrected p = 0.277, Mann-Whitney U test) from the lesion compared to matched cells that were not affected by rotation alignment (Fig. 4b). These findings support our hypothesis that the rotation alignment of histology improved matching for individual cells as their dorso-ventral positions in histology do not significantly differ from non-rotation affected cells following rotation alignment.

Comparing all matched cell pairs with all possible cell pairs that were not matched *post hoc* showed two distinct populations (Fig. 5a,b). 2D Euclidean distances were significantly closer (corrected p < 0.001; one-sided Mann-Whitney U test), and joint PDF values were significantly higher (corrected p < 0.001; one-sided Mann-Whitney U test) for matched cells compared to non-matched cells. Of all matched cells, 2D Euclidean distances and joint PDF values were located outside the 5th and 95th percentile of the distributions, respectively. Jaccard indices of cell soma areas and Jaccard indices of total cell areas were significantly higher for matched cells compared to non-matched cells (both corrected p < 0.001; one-sided Mann-Whitney U tests). Next, we aimed at investigating whether the spatially nearest cell pairs were actually matched. For each cell in *post hoc* histology, we identified the cell in *in vivo* calcium imaging, with the minimum 2D Euclidean distance from that cell, respectively. In every case, the matched cells were found to be closer in 2D Euclidean distance to one another than any
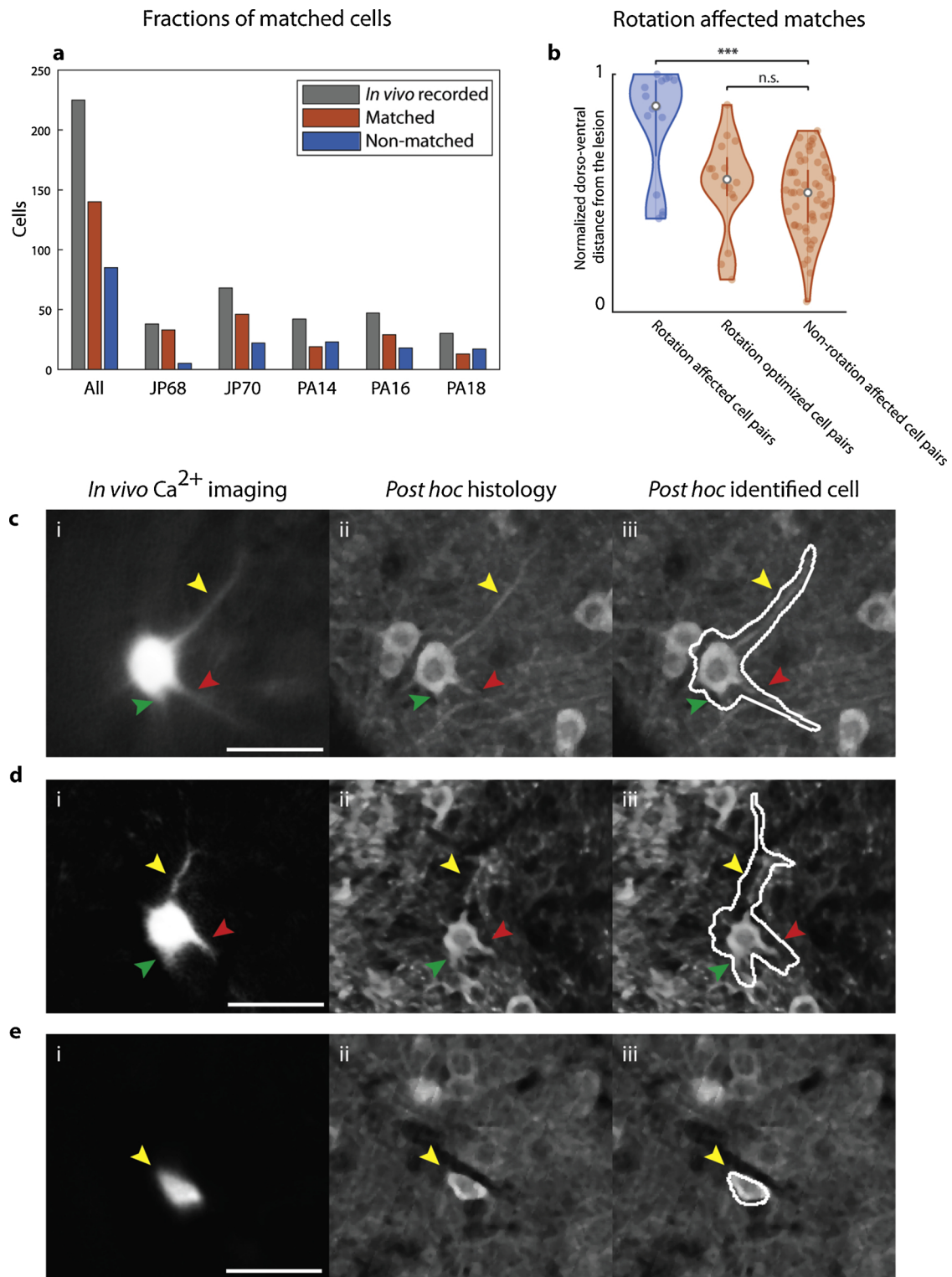
Fig. 4. *in vivo* recorded cells identified in *post hoc* histology. a) Numbers of the cells recorded *in vivo* in all animals and per animal (gray). Fractions of the recorded cells matched (red) and non-matched (blue) *post hoc* for all animals and per animal. b) Optimizing rotation angles of 3D histology in the 2D–3D alignment modifies histological matching partners for a subset of cells recorded *in vivo*. Initial to rotation alignment, this subset of cells were matched to neurons in histology at a greater estimated distance from the lesion (corrected p = 0.006) (blue) compared to matched cells, not affected by rotation alignment (right, red). After rotation alignment (middle, red), no significant difference exists between rotation affected and non-rotation affected cells (corrected p = 0.277). Bonferroni correction was used to account for multiple testing. Mann-Whitney U test was used to compare the distances. c), d), and e) Distinct geometries of individual neurons can be captured in *in vivo* calcium imaging (i) and are preserved in *post hoc* histology (ii, iii). Color-coded arrowheads highlight prominent morphological structures captured *in vivo* and *post mortem*. (iii) White curves are automatically segmented cell shapes derived from *in vivo* calcium imaging. Similarity scores of the matched cell are: c) 0.70 d) 0.44 e) 0.53. All scale bars are 50 μm.
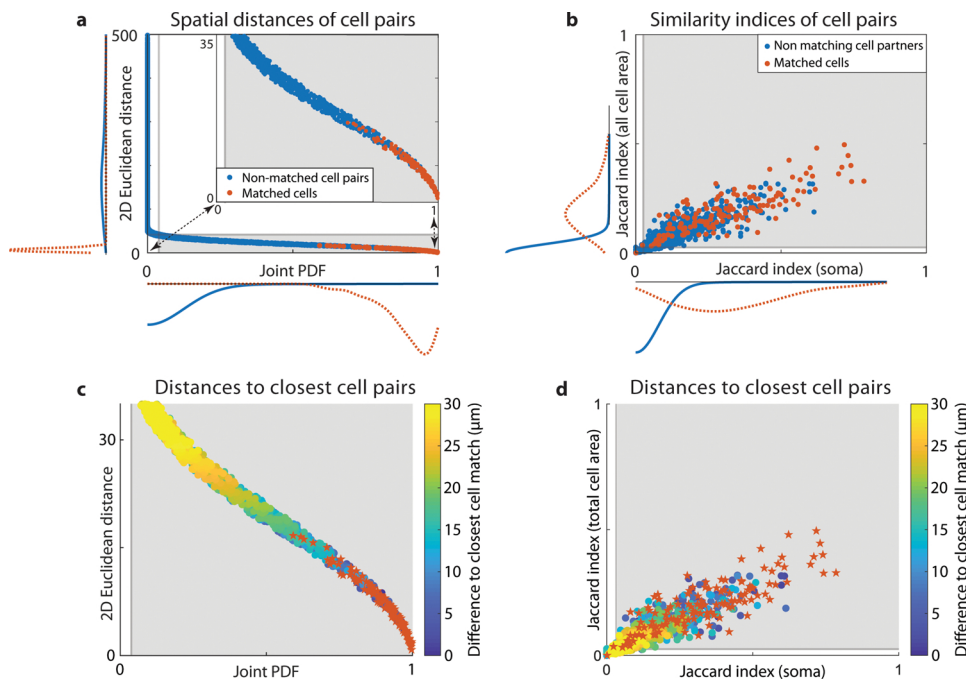
Fig. 5. Post hoc matched and non-matched cells represent separated populations. a) 2D Euclidean distances and joint probability density functions of non-matched (blue) cell pairs (*in vivo* calcium imaging and histology) and matched cell pairs (red) present separated populations. Gray lines depict the 5th and 95th percentiles for 2D Euclidean distances and joint PDFs, respectively. Inset: zoom-in on the 5th and 95th percentiles. b) Jaccard indices of total cell area and soma area of all non-matched cell pairs (blue) and matched cell pairs (red). For a) and b), kernel smoothing functions were used to depict distributions for each axis. c) 2D Euclidean distances and joint probability density functions for cell pairs (as in inset a). d) Jaccard indices of total cell area and soma area of the same cell pairs as in c). *Post hoc* identified cell pairs are indicated by stars (red). All non-matched cell pairs (dots) are color-coded by the 2D Euclidean distances to the closest matching cell candidate in calcium imaging.

other non-matched cell pair. All differences of 2D Euclidean distances are positive, showing that the closest cell pairs were matched (Fig. 5cd).

Comparing *in vivo* recorded cells that were matched *post hoc* in histology with *in vivo* recorded cells that were not matched *post hoc* in histology revealed significantly different cell populations. The cell soma area of non-matched cells was significantly larger in *in vivo* calcium imaging than cell soma area of *post hoc* matched cells (corrected $p = 0.007$, t-test). The eccentricity of *in vivo* recorded cell somata from non-matched cells was not significantly different compared to *post hoc* matched cells (corrected $p = 0.074$, t-test). The similarity scores of matched cells correlated negatively with the size of cell somata ($r = -0.56$, $p < 0.001$), as well as the eccentricity of cell somata ($r = -0.32$, $p < 0.001$). We next investigated whether non-matched cells were rather located at the borders of the field of view. The Euclidean distance of matched and non-matched cells to the spatial centroid of all *in vivo* recorded cells did not show a significant difference (corrected $p = 0.34$, t-test).

3.6. Validation of the cell matching method

For the purpose of validation we undertook a number of approaches: First, we were interested in evaluating the effect of an artificially introduced error on the matching of cells. For one animal, we randomly rotated the *in vivo* acquired calcium imaging data 52 times along the x- and y-axis ($\pm$ 45°) relative to the 3d histology model. With the errors introduced, we matched, on average, 33.54 ± 1.09 (mean $\pm$ Stdev) cells, whereas we matched 34 cells without an error being introduced (Fig. 6a). The number of matched cells with the artificial error being introduced was not significantly different compared to the alignment without an error being introduced (corrected $p = 0.67$, Z-test). As mentioned earlier, 34 cells were matched without the introduction of an artificial error. Following the introduction of artificial errors, 69.23 ± 0.03 % (mean $\pm$ Stdev) of the 34 cells were matched identically in histology. The similarity scores of matched cells following the introduction of the artificial error was 0.51 ± 0.10 and not significantly lower (corrected $p = 0.99$, t-test) than the similarity scores without the introduction of the artificial error 0.52 ± 0.12 (mean $\pm$ Stdev).

Next, we introduced another type of artificial error by randomly rotating the histology model relative to the *in vivo* calcium imaging data

for 52 times along the x- and y-axis ($\pm$ 45°) and evaluated cell matching. In this scenario, we did not optimize the alignment following the introduction of the error. We matched 28.6 ± 2.29 (mean $\pm$ Stdev) cells with random rotations being introduced (Fig. 6b). The distribution of randomly matched cells was significantly lower than the number of cells matched without introduction of a random error (corrected $p = 0.037$, Z-test). The similarity scores of matched cells upon introduction of random errors were 0.50 ± 0.11 (mean $\pm$ Stdev), and did not show a significant difference to similarity scores of matched cells in the configuration without introduction of a random error.

Another scenario we tested was a potential loss of blood vessels due to detection issues during *in vivo* calcium imaging. We investigated the effect of decreased blood vessel identification on the multimodal alignment and cell matching procedure. For this purpose we randomly removed individual connected blood vessel structures to approximate situations with 10 %, 25 %, 50 %, and 70 % of initially detected blood vessels remaining. Following random removing of blood vessels, 9.63 %, 24.05 %, 48.37 %, and 72.91 % of the original pixels of segmented blood vessel structures remained in the corresponding configurations (figure S3). 100 % of blood vessels were represented by 19 individual blood vessel structures and a total contour length of 3.53 mm. Random subsampling of 10 %, 25 %, 50 %, and 70 % of blood vessels resulted in 7, 12, 16, and 17 individual blood vessels, with a total contour length of 0.55 mm, 1.01 mm, 1.99 mm, and 2.85 mm, respectively. Three biologists were asked to perform multimodal alignment using *in vivo* and *post hoc* detected blood vessels. Following alignment, 14.67 ± 6.51 (mean $\pm$ Stdev) cells were matched with approximately 10 %, 17 ± 3.46 (mean $\pm$ Stdev) cells were matched with approximately 25 %, 27.33 ± 6.35 (mean $\pm$ Stdev) cells were matched with approximately 50 %, and 32 ± 1 (mean $\pm$ Stdev) cells were matched with approximately 75 %, of the initially detected blood vessels. 34 cells were matched in the configuration with 100 % of the blood vessels present. For all configurations, we quantified the fraction of the same cell pairs that were matched between *in vivo* calcium imaging and histology compared to the configuration where alignment was achieved using 100 % of the detected blood vessels. Using alignments based on 10 % and 25 % of the blood vessels, none of the matched cell pairs were identical with the cell pairs matched with all blood vessels present. In alignments based on 50 % and 75 % of the blood vessels, 25.81 ± 22.58 % (mean $\pm$ Stdev), and 65.67 ± 2.05 % (mean $\pm$ Stdev), of the

matched cell pairs were identical with the cell pairs matched using 100 % of blood vessels, respectively (Fig. 6c). The confidence (similarity scores) of matched cells significantly increased with the fractions of

blood vessels used for the alignment (Fig. 6d, p < 0.001, one-way ANOVA). The similarity scores of matched cells from alignments based on 10 % of blood vessels did not significantly differ from similarity
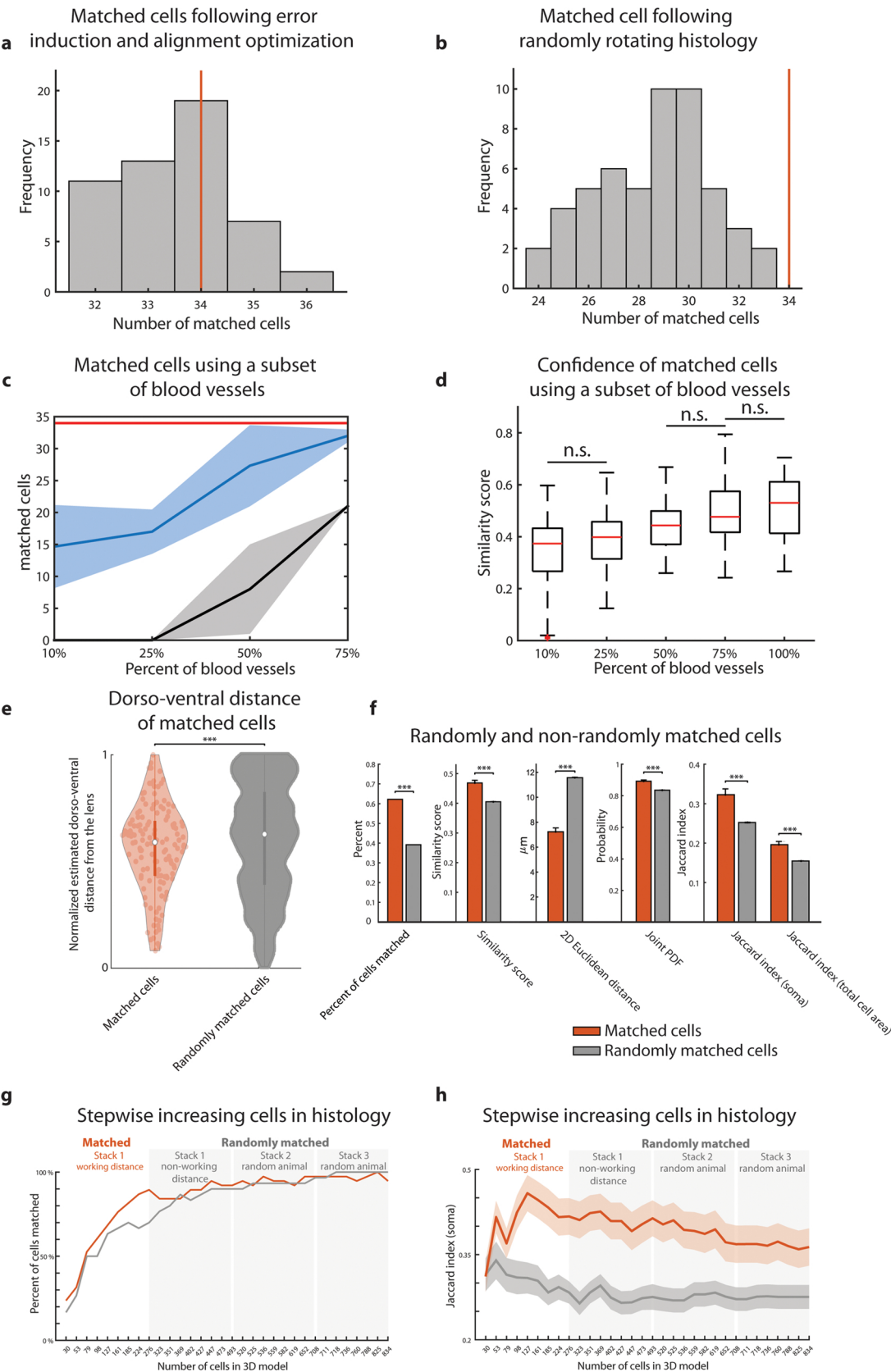
(caption on next page)

Fig. 6. Validation of the cell matching method. a) Alignment and cell matching following the introduction of an artificial error to *in vivo* calcium imaging did not reduce the number of cells matched (corrected p = 0.67, Z-test) compared to alignment without an artificial error (red line, 34 cells). b) Randomly rotating histology resulted in a lower number of cells matched compared to no-rotation (red line, 34 cells). c) Number of matched cells and d) similarity scores increase (p < 0.001, one-way ANOVA) with increased blood vessel structures (all p values in table S1, Tukey-Kramer *post hoc* test). In c), blue traces are the mean and Stdev of matched cells for each configuration. Black traces depict matched cell pairs that are identical with the cell pairs matched using 100 % of blood vessels. 34 matched cells are indicated by the red line in c). e), f) Cells matched at chance level (translating cells in histology 1000 times along the x- and y-axis; grey) differ significantly from non-random configurations (red). e) Normalized dorso-ventral distances of matched cells from the lesion (five animals) have a significantly different variance (corrected p < 0.001, two sample F-test of variance) compared to randomly matched cells. f) Randomly matched cells resulted in a significantly lower fraction of matched cells (X^2-test), at significantly lower similarity scores; significantly higher 2D Euclidean distances; significantly lower joint PDF and Jaccard indices (soma, total cell area) compared to non-random configurations (red bars; all corrected p < 0.001, Mann-Whitney U tests). Bars are mean ± Stdev. g) h) Increasing cell number in histology raised the fraction of matched cells and reduced the 2D Euclidean distance between matched cell pairs. Random configurations - *in vivo* calcium imaging data from a different animal than histology stack 1, 2, 3; grey. Non-random configuration - *in vivo* calcium imaging data from same animal as stack 1; red. Curves and shaded areas depict mean ± SEM.

scores of matched cells from alignments based on 25 % of blood vessels (p = 0.12, Tukey-Kramer test). Further, the similarity scores of matched cells from alignments based on 50 % and 75 % were not significantly different (p = 0.17, Tukey-Kramer test), neither from alignments based on 75 % and 100 % of all blood vessels (p = 0.63, Tukey-Kramer test). Between all other configurations, significant differences between the similarity scores were observed (Fig. 6d; table S1).

Fourth, we evaluated how the number, distances, and morphological similarities of matched cells deviate from chance level. Therefore, we randomly displaced the positions of cells detected in histology 1000 times and evaluated the numbers and similarity metrics of matched cells. We performed the simulation for five animals. For four out of five animals, the number of randomly matched cells was significantly lower in the random configurations compared to standard (non-translated) configurations (corrected p < 0.001 for four animals, Z-test). We pooled data of five animals and compared cell matching results of non-translated and random configurations. The distributions of the normalized estimated dorso-ventral distances from the lesion in *post hoc* histology of matched cells were significantly different in random and non-random configurations (corrected p < 0.001; two sample F-test of variance). In contrast to random configurations, the normalized estimated distances from the lesion of matched cells were approximately normally distributed in non-random configurations (Fig. 6e).

In total, a significantly higher fraction of cells was matched in non-random configurations compared to random configurations (corrected p < 0.001, X^2 test). Matched cells in random configurations differ from matched cells in non-random configurations in all similarity metrics. The similarity score, calculated for each cell pair, was significantly higher in non-random configurations compared to random configurations (corrected p < 0.001, Mann-Whitney U test). Maximized similarity scores indicate that cells matched in the non-random configuration were matched with higher confidence than cells matched at random configurations. 2D Euclidean distances (corrected p < 0.001, Mann-Whitney U test), joint PDF values (corrected p = 0.001, Mann-Whitney U test), and Jaccard indices for cell soma area and total cell area (both corrected p < 0.001, Mann-Whitney U tests) were significantly different between non-random and random configurations (Fig. 6f).

As the density of neurons varies across brain regions we investigated the effects of potential regional cell-density differences on our results. Cell matching between *in vivo* calcium imaging and *post hoc* histology was performed by evaluating two-dimensional parameters We artificially increased the number of cells in histology by combining *post hoc* 3D histology models of three animals, with the highest number of cells, along the dorso-ventral axis. The dorso-ventral size of the 3D model highly correlates with the number of cells in the 3D model (r^2 = 0.995, p < 0.001; Pearson correlation coefficient; figure S4, a). We used the combined 3D histology model and aligned *in vivo* calcium imaging data of two animals. Calcium imaging data of animal 1 was derived from the same animal as stack 1 of the combined model. Stack 1 was divided along the dorso-ventral axis into the working distance and non-working distance segments. The working distance segment represented the

histological volume that was imaged *in vivo* with the miniscope in animal 1, assuming that cells to be matched *post hoc* were above chance level for animal 1. Calcium imaging data of animal 2 was different from all 3D histology stacks of the combined model, resembling random configuration in all segments of the combined *post hoc* histology 3D model.

Within stack 1 (working distance), the percentage of cells matched was higher for animal 1 than for animal 2. In random configurations (stack 1 (non-working distance), stack 2, and stack 3), the fractions of matched cells overlapped and converged towards 100 % within stack 3 for both animals (Fig. 6g). Increasing the number of cells in the *post hoc* histology model decreased the 2D Euclidean distance between matched cell pairs. Within the working distance of the miniscope of stack 1, the 2D Euclidean distance was lower for animal 1 than for animal 2. The 2D Euclidean distance converges in both configurations (non-random – animal 1 and random – animal 2) with increasing cell number (figure S4, b). In contrast to the 2D Euclidean distances, the Jaccard index of cell soma area remains sustained with increasing cell numbers for animal 1 compared to animal 2 (Fig. 6h)

4. Discussion

Neuronal cell types are linked to their anatomy, function, and specific expression of molecular markers that help to understand neuronal contributions to cognitive processes in rodents during natural behavior. Current approaches that combine the recording of neuronal activity with the identification of their histological profiles during freely moving behavior are limited. In this study, we present a novel method to semi-automatically identify cells in *post hoc* histology, following one-photon calcium imaging in freely moving animals. Our approach is based on the co-registration of 2D *in vivo* acquired images and a reconstructed 3D model of the brain structure, derived from multiple 3D scanned histological brain sections. In *post hoc* histology, cell-type-specific discrimination can be performed by immunohistochemical labeling, and neuroanatomical tracers can visualize the connectivity of *in vivo* recorded neurons. Our method facilitates further insights into the functional architecture of the cortex during freely moving behavior by combining information of topographic specificity (localizing recorded cells), with cell-type specificity (neuronal identity using immunohistochemistry), and functional specificity (functional calcium imaging).

Despite matching *in vivo* recorded cells in *post hoc* histology, neuronal subtype-specific investigations can be specified *a priori* by controlling the expression of calcium reporters. This can be achieved by viral vectors with cell-type-specific promoters (Chhatwal et al., 2007), serotypes (Shevtsova et al., 2005), or by genetically modified animal lines (Daigle et al., 2018). However, antibody-based labeling provides a greater variety and selectivity in neuronal identification. Another problem arises when cre-based transgene expression is not binary throughout development (Sjulson et al., 2016), or when only limited genetically modified animal lines are available in the desired species (He and Huang, 2018). For these reasons, we aimed at matching *in vivo*

recorded cells in *post hoc* histology for determining neuronal-subtypes with immunohistochemical labeling *post hoc*.

Manual re-mounting of the miniscope to the head of the animal at the beginning of each recording session required the alignment of the cells detected across individual calcium imaging sessions. We observed that aligning individual recordings based on spatial arrangements of neuronal footprints can be misleading due to variations in the number of recorded cells in each recording session (Ziv et al., 2013) and ambiguous patterns of neuronal footprints caused due to focus dependent magnifications in the field of view. Therefore, we aligned calcium imaging recordings semi-automatically by using projection images, resembling anatomical landmarks, and detected the same cells across recordings automatically. Combined multiple calcium imaging experiments showed that different subsets of neurons were detected in individual experiments (Fig. 1a) with the majority of the cells (41 %) being recorded on a single day. Previously, cells were tracked manually (Grewe et al., 2017; Mau et al., 2018) and automatically (Sheintuch et al., 2017) using a Bayesian model. In contrast to the latter, we estimate the kernel size for calculating PDFs that resemble the likelihood of the somatic centroid automatically and identify cells across experiments automatically by determining maximum joint PDFs.

In order to re-identify miniscope image planes in 3D histology *post hoc*, the co-registration of two consecutive 70 μm thick brain sections in three out of five experiments was required. We cut histological specimens parallel to the imaging plane (axial) to minimize the number of co-registration procedures required for reconstruction, as this step was the most time-consuming procedure and ranged from 4 to 15 h. In contrast to our method, 3D histology reconstruction, following *in vivo* calcium imaging, has been performed by co-registering brain sections, cut perpendicular to the *in vivo* acquired imaging plane. This leads to a higher number of sections that need to be co-registered (Langer and Helmchen, 2012), possibly resulting in a higher loss of tissue along the brain section borders. *Post hoc* matched cells were mainly found to be located in the center along the axial distance within the histological 3D models (Fig. 6e). Due to the implantation of the endoscopic relay GRIN lens, brain tissue can be compressed, and edema may occur, leading to the formation of scar tissue and inflammatory processes (Levene et al., 2004). Following extraction of the endoscopic relay GRIN lenses and cutting of histological sections, we observed a localized loss of tissue, likely due to potential inflammatory processes and necrotic tissue. For combining *in vivo* calcium imaging and *post hoc* histology, the structure of local blood vessels served as anatomical landmarks. We propose a semi-automatic image registration approach for co-registering 2D (*in vivo*) to 3D (*post hoc*) acquired imaging data and automatically maximize matching by determining rotation angles of *post hoc* histology relative to *in vivo* acquired images. Non-optimized rotations resulted in z-distance dependent offsets of matching *in vivo* recorded cells *post hoc* in histology. In experiments with rotation angle offsets, the optimization procedure modified the pairing of a subset of *post hoc* matched cell pairs. These cells were initially matched to a population of cells in 3D histology models, at a systematically higher distance from the lesion, compared to all other matched cells. Following rotation alignment, the systematic differences vanished (Fig. 4b). The time spent for semi-automatic multimodal image alignment ranged from 1 to 2 h. We improved blood vessel based co-registration upon earlier versions that relied on time-consuming manual co-registration of volumetric scans, acquired *in vivo* and *post hoc* (Kerlin et al., 2010; Ko et al., 2011; Langer and Helmchen, 2012).

In vivo recorded cells were reliably matched in *post hoc* histology at a high fraction (∼ 60 %), with some variations across animals (Fig. 4a). Importantly, we matched *in vivo* recorded cells *post hoc* in all animals, showing that our method could reliably be applied across animals. We provide similarity values as a measure for confidence for each *post hoc* matched cell. For a subset of matched cells, their characteristic shapes, captured *in vivo* and *post hoc*, were preserved. This provides strong evidence at a single-cell level that these cells were unambiguously

matched *post hoc* (Fig. 4c–e). About 40 % of *in vivo* recorded cells were not matched *post hoc*. Non-matched cells show significantly enlarged detected somatic cell sizes compared to *post hoc* matched cells. These cells are likely located in out of focus regions during *in vivo* calcium imaging. We observed a significant negative correlation between somatic cell size and similarity scores, indicating that cells with a small soma areas were matched with higher confidence compared to cells with enlarged somatic areas. A significant negative correlation was found as well for the eccentricity of somatic shapes and similarity scores, supporting that cell somata with a circular structure were matched *post hoc* with higher confidence. The circular appearance of cell somata is biased due to the optical aberrations of endoscopic GRIN lenses. Loss of brain tissue due to the cutting process and inflammatory processes also limited the number of cells matched *post hoc*. We would expect that newer improved versions of miniscopes with electronic focusing and implantation of GRIN lenses in mice (decreased blood volume allows easier GRIN lens implantation and results in smaller tissue disruptions) would allow higher matching rates. In comparison to imaging cortical neurons with non-invasive 2 P M during head fixation without relay GRIN lenses, does not necessitate automatic cell matching *post hoc* (Kerlin et al., 2010; Kuhlman et al., 2013; Langer and Helmchen, 2012; Weiler et al., 2018). 2 P M results in a significantly higher optical resolution and has the ability to acquire volumetric scans in contrast to one-photon miniscopes (Glas et al., 2019). This resulted in a higher fraction of cells matched in *post hoc* histology (about 80 %) and with an increasing amount of time spent up to 95 % to 100 %. Reported times spent on manual multimodal alignment and cell identification ranges from 4 to 50 h (Kerlin et al., 2010; Langer and Helmchen, 2012), which is significantly higher than our most time-consuming procedure, the co-registration of consecutive histological sections.

We performed several simulation studies to validate our method. Firstly, following the introduction of artificial errors to *in vivo* calcium imaging data and preceding image registration, 69 % of initially matched cell pairs (without an artificial random error being introduced) were matched identical following the introduction of artificial random errors (Fig. 6a). Secondly, following the introduction of artificial errors to histology by rotating it arbitrarily relative to *in vivo* calcium imaging data, a significantly lower number of cells was matched *post hoc*. Thirdly, we quantified the effect of missing blood vessels in *in vivo* calcium imaging on the matching cells *post hoc*. We showed that the confidence for matching cells as well as the number of matched cells decline with a decreasing number of blood vessels detected *in vivo*. We concluded that performing multimodal image alignment using 17 *in vivo detected* blood vessels (total contour length 2.85 mm, 75 % of all blood vessels) were sufficient enough to match about 66 % of the same cell pairs that were matched using 19 *in vivo* detected blood vessels (total contour length 3.53 mm, 100 % of the blood vessels) (Fig. 6c). Fourthly, we showed that the numbers of matched cells, as well as their spatial distance and similarities of their shapes, were above chance level. Fifthly, as the density of neurons varies across brain regions, we simulated cell matching with varying numbers of cells in histology. As expected, increasing cell numbers in histology resulted in a higher number of cells matched *post hoc*. 2D Euclidean distances between the cell pairs declined with increasing cells in histology. However, the shape similarity of somatic regions remained sustained for non-randomly matched cells compared to randomly matched cells with increasing cell number in histology.

5. Conclusion

In this study, we propose a new method to semi-automatically identify neurons, recorded with a miniature one-photon microscope in freely moving rats, in *post hoc* fixed brain sections. The method provides a new tool for a comprehensive understanding of neuronal circuits during freely moving behavior by bridging the gap between the functional activity of neurons, captured by *in vivo* calcium imaging, their

diversity of neuronal cell-types, determined by *post hoc* immunohistochemistry, and their underlying network of neuronal connections, studied with neuroanatomical tracers. Current approaches for such comprehensive investigations during freely moving behavior are technically limited, time-intensive, and costly. *Post hoc* immunolabeling allows precise cell-type classification with a multitude of immunohistochemical markers applied consecutively. In our experiments, we matched reliably 60 % of *in vivo* recorded cells *post hoc* with our cell matching algorithm. We provided evidence that *post hoc* matched cells showed, despite the high number of possible matching candidates in *post hoc* histology, significantly better cell similarity metrics compared to matched cells at chance level.

Ethical standards agreement

Funding

CRediT authorship contribution statement

Philip Anner: Investigation, Software, Validation, Formal analysis, Writing, Visualization. **Johannes Passecker:** Investigation, Methodology, Writing - review & editing. **Thomas Klausberger:** Conceptualization, Resources, Funding acquisition, Writing - review & editing, Supervision. **Georg Dorffner:** Conceptualization, Resources, Funding acquisition, Writing - review & editing, Supervision.

Declaration of Competing Interest

None.

Acknowledgments

Appendix A. Supplementary data

Supplementary material related to this article can be found, in the online version, at doi:https://doi.org/10.1016/j.jneumeth.2020.108765.

References

Chen, T.-W., Wardill, T.J., Sun, Y., Pulver, S.R., Renninger, S.L., Baohan, A., Schreiter, E.R., Kerr, R.A., Orger, M.B., Jayaraman, V., Looger, L.L., Svoboda, K., Kim, D.S., 2013. Ultrasensitive fluorescent proteins for imaging neuronal activity. Nature 499, 295–300. https://doi.org/10.1038/nature12354.

Chhatwal, J.P., Hammack, S.E., Jasnow, A.M., Rainnie, D.G., Ressler, K.J., 2007. Identification of cell-type-specific promoters within the brain using lentiviral vectors. Gene Ther. 14, 575–583. https://doi.org/10.1038/sj.gt.3302898.

Daigle, T.L., Madisen, L., Hage, T.A., Valley, M.T., Knoblich, U., Larsen, R.S., Takeno, M.M., Huang, L., Gu, H., Larsen, R., Mills, M., Bosma-Moody, A., Siverts, L.A., Walker, M., Graybuck, L.T., Yao, Z., Fong, O., Nguyen, T.N., Garren, E., Lenz, G.H., Chavarha, M., Pendergraft, J., Harrington, J., Hirokawa, K.E., Harris, J.A., Nicovich, P.R., McGraw, M.J., Ollerenshaw, D.R., Smith, K.A., Baker, C.A., Ting, J.T., Sunkin, S.M., Lecoq, J., Lin, M.Z., Boyden, E.S., Murphy, G.J., da Costa, N.M., Waters, J., Li, L., Tasic, B., Zeng, H., 2018. A suite of transgenic driver and reporter mouse lines with enhanced brain-cell-Type targeting and functionality. Cell 174, 465–480. https://doi.org/10.1016/j.cell.2018.06.035. e22.

DeFelipe, J., Fariñas, I., 1992. The pyramidal neuron of the cerebral cortex: morphological and chemical characteristics of the synaptic inputs. Prog. Neurobiol. 39, 563–607. https://doi.org/10.1016/0301-0082(92)90015-7.

DeFelipe, J., López-Cruz, P.L., Benavides-Piccione, R., Bielza, C., Larrañaga, P., Anderson, S., Burkhalter, A., Cauli, B., Fairén, A., Feldmeyer, D., Fishell, G., Fitzpatrick, D., Freund, T.F., González-Burgos, G., Hestrin, S., Hill, S., Hof, P.R., Huang, J., Jones, E.G., Kawaguchi, Y., Kisvárday, Z., Kubota, Y., Lewis, D.A., Marín, O., Markram, H., McBain, C.J., Meyer, H.S., Monyer, H., Nelson, S.B., Rockland, K., Rossier, J., Rubenstein, J.L.R., Rudy, B., Scanziani, M., Shepherd, G.M., Sherwood, C.C., Staiger, J.F., Tamás, G., Thomson, A., Wang, Y., Yuste, R., Ascoli, G.A., 2013. New insights into the classification and nomenclature of cortical GABAergic interneurons. Nat. Rev. Neurosci. 14, 202–216. https://doi.org/10.1038/nrn3444.

Frangi, A.F., Niessen, W.J., Vincken, K.L., Viergever, M.A., 1998. Multiscale Vessel Enhancement Filtering, in: Medical Image Computing and Computer-assisted Interveention- MICCAI. Lecture Notes in Computer Science, Berlin, pp. 130–137. https://doi.org/10.1007/BFb0056195.

Glas, A., Hübener, M., Bonhoeffer, T., Goltstein, P.M., 2019. Benchmarking miniaturized microscopy against two-photon calcium imaging using single-cell orientation tuning in mouse visual cortex. PLoS One 14, e0214954. https://doi.org/10.1371/journal.pone.0214954.

Grewe, B.F., Gründemann, J., Kitch, L.J., Lecoq, J.A., Parker, J.G., Marshall, J.D., Larkin, M.C., Jercog, P.E., Grenier, F., Li, J.Z., Lüthi, A., Schnitzer, M.J., 2017. Neural ensemble dynamics underlying a long-term associative memory. Nature 543, 670–675. https://doi.org/10.1038/nature21682.

Grienberger, C., Konnerth, A., 2012. Imaging calcium in neurons. Neuron 73, 862–885. https://doi.org/10.1016/j.neuron.2012.02.011.

He, M., Huang, Z.J., 2018. Genetic approaches to access cell types in mammalian nervous systems. Curr. Opin. Neurobiol. 50, 109–118. https://doi.org/10.1016/j.conb.2018.02.003.

Iannaccone, P.M., Jacob, H.J., 2009. Rats!. Dis. Model. Mech. 2, 206–210. https://doi.org/10.1242/dmm.002733.

Jung, J.C., Schnitzer, M.J., 2003. Multiphoton endoscopy. Opt. Lett. 28, 902. https://doi.org/10.1364/OL.28.000902.

Keller, A.J., Martin, K.A.C., 2015. Local Circuits for Contrast Normalization and Adaptation Investigated with Two-Photon Imaging in Cat Primary Visual Cortex. J. Neurosci. 35, 10078–10087. https://doi.org/10.1523/JNEUROSCI.0906-15.2015.

Kellner, D., 2011. Region Growing (2D/3D grayscale).

Kepecs, A., Fishell, G., 2014. Interneuron cell types are fit to function. Nature 505, 318–326. https://doi.org/10.1038/nature12983.

Kerlin, A.M., Andermann, M.L., Berezovskii, V.K., Reid, R.C., 2010. Broadly tuned response properties of diverse inhibitory neuron subtypes in mouse visual cortex. Neuron 67, 858–871. https://doi.org/10.1016/j.neuron.2010.08.002.

Khan, A.G., Poort, J., Chadwick, A., Blot, A., Sahani, M., Mrsic-Flogel, T.D., Hofer, S.B., 2018. Distinct learning-induced changes in stimulus selectivity and interactions of GABAergic interneuron classes in visual cortex. Nat. Neurosci. 21, 851–859. https://doi.org/10.1038/s41593-018-0143-z.

Kiessling, F., Pichler, B.J. (Eds.), 2011. Small Animal Imaging. Springer Berlin Heidelberg, Berlin, Heidelberg. https://doi.org/10.1007/978-3-642-12945-2.

Ko, H., Hofer, S.B., Pichler, B., Buchanan, K.A., Sjöström, P.J., Mrsic-Flogel, T.D., 2011. Functional specificity of local synaptic connections in neocortical networks. Nature 473, 87–91. https://doi.org/10.1038/nature09880.

Kuhlman, S.J., Olivas, N.D., Tring, E., Ikrar, T., Xu, X., Trachtenberg, J.T., 2013. A disinhibitory microcircuit initiates critical-period plasticity in the visual cortex. Nature 501, 543–546. https://doi.org/10.1038/nature12485.

Langer, D., Helmchen, F., 2012. Post hoc immunostaining of GABAergic neuronal subtypes following in vivo two-photon calcium imaging in mouse neocortex. Pflügers Arch. - Eur. J. Physiol. 463, 339–354. https://doi.org/10.1007/s00424-011-1048-9.

Lapray, D., Lasztoczi, B., Lagler, M., Viney, T.J., Katona, L., Valenti, O., Hartwich, K., Borhegyi, Z., Somogyi, P., Klausberger, T., 2012. Behavior-dependent specialization of identified hippocampal interneurons. Nat. Neurosci. 15, 1265–1271. https://doi.org/10.1038/nn.3176.

Levene, M.J., Dombeck, D.A., Kasischke, K.A., Molloy, R.P., Webb, W.W., 2004. In vivo Multiphoton Microscopy of Deep Brain Tissue. J. Neurophysiol. 91, 1908–1912. https://doi.org/10.1152/jn.01007.2003.

Markram, H., Toledo-Rodriguez, M., Wang, Y., Gupta, A., Silberberg, G., Wu, C., 2004. Interneurons of the neocortical inhibitory system. Nat. Rev. Neurosci. 5, 793–807. https://doi.org/10.1038/nrn1519.

Mau, W., Sullivan, D.W., Kinsky, N.R., Hasselmo, M.E., Howard, M.W., Eichenbaum, H., 2018. The same hippocampal CA1 population simultaneously codes temporal information over multiple timescales. Curr. Biol. 28, 1499–1508. https://doi.org/10.1016/j.cub.2018.03.051. e4.

Mukamel, E.A., Nimmerjahn, A., Schnitzer, M.J., 2009. Automated analysis of cellular signals from large-scale calcium imaging data. Neuron 63, 747–760. https://doi.org/10.1016/j.neuron.2009.08.009.

O'Keefe, J., Dostrovsky, J., 1971. The hippocampus as a spatial map. Preliminary evidence from unit activity in the freely-moving rat. Brain Res. 34, 171–175. https://doi.org/10.1016/0006-8993(71)90358-1.

Pinault, D., 1996. A novel single-cell staining procedure performed in vivo under electrophysiological control: morpho-functional features of juxtacellularly labeled thalamic cells and other central neurons with biocytin or Neurobiotin. J. Neurosci. Methods 65, 113–136. https://doi.org/10.1016/0165-0270(95)00144-1.

Rueckert, D., Sonoda, L.I., Hayes, C., Hill, D.L., Leach, M.O., Hawkes, D.J., 1999. Nonrigid registration using free-form deformations: application to breast MR images. IEEE Trans. Med. Imaging 18, 712–721. https://doi.org/10.1109/42.796284.

Sheintuch, L., Rubin, A., Brande-Eilat, N., Geva, N., Sadeh, N., Pinchasof, O., Ziv, Y., 2017. Tracking the same neurons across multiple days in Ca2+ imaging data. Cell Rep. 21, 1102–1115. https://doi.org/10.1016/j.celrep.2017.10.013.

Shevtsova, Z., Malik, J.M.I., Michel, U., Bähr, M., Kügler, S., 2005. Promoters and serotypes: targeting of adeno-associated virus vectors for gene transfer in the rat central

nervous system in vitro and in vivo. Exp. Physiol. 90, 53–59. https://doi.org/10.1113/expphysiol.2004.028159.

Sjulson, L., Cassataro, D., DasGupta, S., Miesenböck, G., 2016. Cell-specific targeting of genetically encoded tools for neuroscience. Annu. Rev. Genet. 50, 571–594. https://doi.org/10.1146/annurev-genet-120215-035011.

Tang, Q., Brecht, M., Burgalossi, A., 2014. Juxtacellular recording and morphological identification of single neurons in freely moving rats. Nat. Protoc. 9, 2369–2381. https://doi.org/10.1038/nprot.2014.161.

Weiler, S., Bauer, J., Hübener, M., Bonhoeffer, T., Rose, T., Scheuss, V., 2018. High-yield in vitro recordings from neurons functionally characterized in vivo. Nat. Protoc. 13, 1275–1293. https://doi.org/10.1038/nprot.2018.026.

Wilson, D.E., Smith, G.B., Jacob, A.L., Walker, T., Dimidschstein, J., Fishell, G., Fitzpatrick, D., 2017. GABAergic Neurons in Ferret Visual Cortex Participate in Functionally Specific Networks. Neuron 93, 1058–1065. https://doi.org/10.1016/j.neuron.2017.02.035. e4.

Zeng, H., Sanes, J.R., 2017. Neuronal cell-type classification: challenges, opportunities and the path forward. Nat. Rev. Neurosci. 18, 530–546. https://doi.org/10.1038/nrn.2017.85.

Ziv, Y., Ghosh, K.K., 2015. Miniature microscopes for large-scale imaging of neuronal activity in freely behaving rodents. Curr. Opin. Neurobiol. 32, 141–147. https://doi.org/10.1016/j.conb.2015.04.001.

Ziv, Y., Burns, L.D., Cocker, E.D., Hamel, E.O., Ghosh, K.K., Kitch, L.J., Gamal, A.El, Schnitzer, M.J., 2013. Long-term dynamics of CA1 hippocampal place codes. Nat. Neurosci. 16, 264–266. https://doi.org/10.1038/nn.3329.